DUET: A Novel Energy Yield Model With 3-D Shading for Bifacial Photovoltaic Systems

Annie C. J. Russell, Christopher E. Valdivia, Cédric Bohémier, Joan E. Haysom, and Karin Hinzer, *Senior Member, IEEE*

***Abstract*—Bifacial photovoltaic (PV) performance models strive to accurately quantify rear-incident irradiance. While ray tracing models are optically rigorous, they require significant computational resources; faster view factor (VF) models are widely adopted but require user-defined loss factors to approximate rear shading and irradiance nonuniformity, introducing uncertainty in energy yield predictions. This article describes DUET—a bifacial PV performance model that calculates optical and electrical performance based on a physically representative array geometry. DUET's novel shading algorithm pairs a 3-D VF model with deterministic ray-object intersections to capture 2-D shade-inclusive irradiance profiles while minimizing computational cost. Series and parallel combination of current–voltage curves capture irradiance nonuniformity throughout the module and array. This article provides validation against open-access system measurements from a test site in Roskilde, Denmark, and comparison to other software tested there [1]. DUET's modeled bifacial energy yield agrees with measured data within −1.56% for fixed-tilt and −0.65% for horizontal single-axis tracked (HSAT) systems. Mean absolute error (MAE) in hourly bifacial power is 14.2–15.0 mW/Wp for fixed-tilt and 17.3–18.3 mW/Wp for HSAT, depending on the module temperature model applied. Comparing modeled and measured rear irradiance of two rear-facing pyranometers, DUET's MAE values of 2.8 W/m^2 for fixed-tilt and 3.7 W/m^2 for HSAT are among the lowest errors reported for other software tested at this site. DUET provides computationally efficient bifacial performance modeling with geographic, temporal, and structural specificity to determine loss factors for use in other performance models or to be used directly in system design optimization.**

***Index Terms*—Albedo, bifacial, diffuse, electrical mismatch, energy yield, irradiance, photovoltaic (PV), ray tracing, shading.**

I. Introduction

BIFACIAL photovoltaic (PV) modules convert both front- and rear-incident light into electrical energy. The rear contribution leads to higher energy yields as compared to traditional one-sided, or *monofacial*, modules. This additional energy can reduce a system's levelized cost of energy, particularly when paired with horizontal single axis tracking (HSAT) [2]. However, uncertainty in bifacial yield prediction can impede design optimization and create a financial risk to project ownership [3]. The exact irradiance incident on the rear of a module depends on a complex set of factors such as the ratio of diffuse to direct light, the properties of the ground cover, and the position and shape of mounting structures [4]. In the absence of validated and accessible bifacial PV performance models and parameters, this complexity would manifest as uncertainty in rear irradiance modeling and inaccuracy in energy yield predictions, system costing, and forecasting.

Significant efforts are underway to increase confidence in bifacial PV modeling accuracy: existing software have undergone validation against field data [4]–[11]; cross-software comparisons provide technical and performance insights [1], [12]–[19]; and open-access field data is available in [20]–[22]. Despite these efforts, many optical models lack either computational efficiency or geographic and temporal specificity. For instance, annual calculations of hourly irradiance in ray tracing models [9]–[11], [14], [15], [17], [18], [23]–[25] typically exceed 12-h run times for HSAT systems unless high-performance computational resources are used [1]. These computationally intensive models capture complex shading and reflection by following a large collection of stochastic rays through multiple interactions with textured surfaces. Conversely, view factor (VF) models can efficiently compute the transfer of radiation between meshed surfaces in a scene [26] but treat shading more simply. While 2-D VF models [5]–[7], [24], [27]–[33] can simulate annual insolation in less than 5 min [1], they require user-defined loss factors to account for structure shade and irradiance nonuniformity along the width of a module or row. However, the geographic- and temporal-specificity of these loss parameters is still not well understood, leading to uncertainty in yield projections [1], [17], [34]. Three-dimensional (3-D) VF models [16], [35]–[38] inherently capture irradiance nonuniformity along the width of a module or row, and while BIGEYE [19], [35], [36] includes object shading, 3-D VF models typically rely on annualized, estimated factors to represent the effect of these structures. MobiDiG Hybrid [8], [24] computes front irradiance with VF and rear irradiance by ray tracing to improve computational efficiency while maintaining array design specificity.

Manuscript received 3 February 2022; revised 26 April 2022; accepted 13 June 2022. Date of publication 4 July 2022; date of current version 28 November 2022. This work was supported by the Natural Sciences and Engineering Research Council of Canada under Grant NSERC CREATE 497981 and Grant STPGP 521894. *(Corresponding author: Annie C. J. Russell.)*

Annie C. J. Russell, Christopher E. Valdivia, Cédric Bohémier, and Karin Hinzer are with SUNLAB, Centre for Research in Photonics, School of Electrical Engineering and Computer Science, University of Ottawa, Ottawa, ON K1N 6N5, Canada (e-mail: aruss100@uottawa.ca; valdivia@uottawa.ca; cbohe083@uottawa.ca; khinzer@uottawa.ca).

Joan E. Haysom is with SUNLAB, Centre for Research in Photonics, School of Electrical Engineering and Computer Science, University of Ottawa, Ottawa, ON K1N 6N5, Canada, and also with the J. L. Richards and Associates Ltd., Kingston, ON K7L 5N4, Canada (e-mail: jhaysom@jlrichards.ca).

Color versions of one or more figures in this article are available at https://doi.org/10.1109/JPHOTOV.2022.3185546.

Digital Object Identifier 10.1109/JPHOTOV.2022.3185546

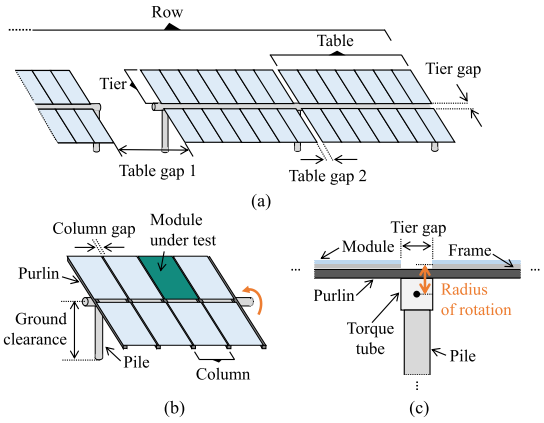

Fig. 1. Selection of DUET's input design parameters illustrated for: (a) row features and (b) table features in a generic 2-in-portrait (2P) system. (c) A close-up cross-section of a 2P system torque tube with user-defined features shown.

This article outlines our approach to fill the efficiency-specificity gap—Dual-sided Energy Tracer (DUET)—a numerical PV performance software with integrated optical and electrical models [39]–[41]. The optical model enhances the 3-D VF approach by checking a finite number of deterministic rays for intersection with objects in the scene and generates shade-inclusive 2-D front and rear module irradiance profiles. The electrical model captures current mismatch losses induced by irradiance nonuniformity across cells and provides module-, string-, or array-level energy yields based on a flexible wiring architecture. DUET is currently under active development in-house and was one of 13 models in the International Energy Agency (IEA) PV Power systems Programme (PVPS) Task 13 bifacial PV modeling comparison [12]. The following sections provide a detailed description of DUET and demonstrate field validation for fixed-tilt and HSAT systems at a test site in Denmark [22]. A list of symbols is available in Table I.

II. DUET Energy Yield Software

The DUET software computes the energy yield of monofacial and bifacial PV modules within a fixed-tilt or HSAT array. The array sits on a flat ground surface with time-varying albedo, ρ, and can consist of any number of rows, tables per row, and tiers or columns of modules per table. The optical model processes hourly or sub-hourly solar resource and meteorological data for the given geographic location. For each simulation, the user selects a single module under test from within the array and defines inputs relating to geography, array and table design, and optical and electrical parameters. A selection of the user-specified features in a row and table is illustrated in Fig. 1 and Table II.

The software separates the simulation into time-independent and time-dependent calculations [see Fig. 2(b) and (c)], the latter with hourly or sub-hourly timestamps. The novel shade model pairs ray-object intersection algorithms with the 3-D VF approach to generate detailed 2-D front and rear irradiance profiles for the selected module. The electrical model then calculates current–voltage (*IV*) curves for each cell and combines cell *IV* curves based on a user-specified wiring architecture to generate the module *IV* curve, including the effect of bypass diodes. Users can simulate multiple modules to construct *IV* curves for multimodule strings and arrays.

DUET provides cell- and module-level outputs for each timestamp as illustrated in Fig. 2(d), including: front and rear average irradiance, 2-D irradiance profiles, module average temperature, cell and module *IV* curves, maximum power, electrical mismatch, and bifacial gain. From these outputs, users can compute the loss factors required for use in 2-D VF models. The following sections provide further details on the DUET algorithm summarized in Fig. 2.

A. Optical Model

The optical model computes front and rear module irradiance based on three irradiance sources: direct radiation from the sun beam, anisotropic diffuse radiation from the sky, and reflected radiation from the ground. As in other 3-D VF models, the diffuse sky dome, ground, and module under test are meshed into patches to facilitate energy transfer calculations. After meshing, the HSAT module patch coordinates are rotated each timestamp based on tracker tilt. The energy that is emitted from one patch and incident on another depends on the area of the irradiated patch, the angle of incidence (AOI), and the solid angle between irradiated and emitting patches. In DUET, an object in the array can partially or completely attenuate energy transfer between two patches if it intersects with the ray that links the patch centroids. The resulting irradiance at the center of each module patch forms the module irradiance profile.

1) Shading Algorithm: The complex shading objects in a modern PV array, such as adjacent rows, mounting structures, and module frame, can be approximated by the combination of the three basic shapes, or *primitives* as shown in Fig. 3(a). These primitives consist of polygons, cylinders, and rectangular prisms. DUET uses ray-primitive intersection routines [42]–[45] to check whether a ray that links the centroids of an emitting source (e) and an irradiated patch (i) intersects with shading objects in the scene.

An intersection indicates that the emitting source may be obscured by a shading object, and we apply a multiplicative shading factor, $\delta_{e,i}$, to the ray's incident irradiance based on the transparency of the intersecting primitive. Intersection with an opaque primitive, such as the cylinder that forms the torque tube in Fig. 3(b), sets $\delta_{e,i}$ to zero. Intersection with a semi-transparent primitive sets $\delta_{e,i}$ to the pre-calculated transparency of the primitive, effectively dimming the ray. For example, the transparency of a polygon that represents a portion of a table is found as the fraction of the associated area that is covered by solar cells, adjusted for the given AOI to account for Fresnel transmittance of an air-to-glass and glass-to-air boundary. If no ray-primitive intersection is found, or if the ray intersects with a transparent primitive such as a a polygon representing a table gap or tier gap, $\delta_{e,i}$ is set to 1. Similarly, the model represents frame shading by setting $\delta_{e,i}$ to 0 for any rear-incident ray that does not pass through the transparent polygon formed by the innermost frame edges.

To decrease computation time, primitives are grouped into a hierarchy of bounding boxes around individual rows, sets of

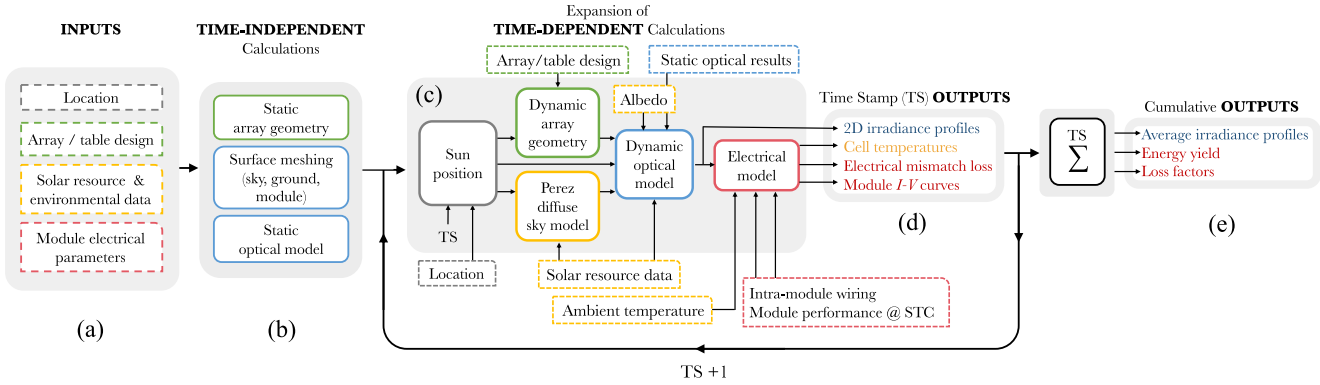

Fig. 2. Block diagram of DUET algorithm for module under test: (a) summary of inputs, (b) time-independent calculations, (c) expansion of time-dependent calculations, (d) timestamp outputs, and (e) cumulative outputs. TS = timestamp; STC = Standard Test Conditions; Grey = geography; green = array/table design; yellow = solar resource & environment; blue = optical model; red = electrical model.

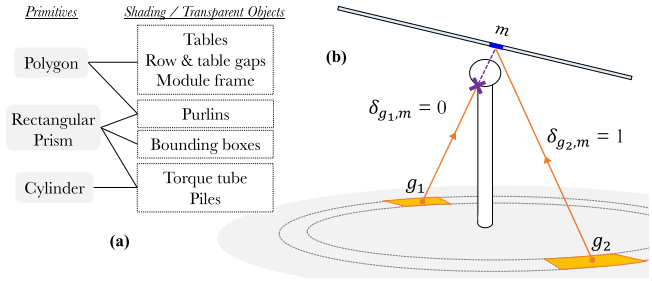

Fig. 3. (a) Composition of shading and transparent objects from primitives. (b) Cross-section of a single axis tracker with shading factors ($\delta_{g_1,m}$ and $\delta_{g_2,m}$) link emitting ground patches, g_1 (obscured) and g_2 (not obscured) with module patch m.

rows, and the full array. The extreme coordinates of the array or row form the corners of these boxes, and DUET checks rays for intersection with successively smaller bounding boxes until only the remaining eligible rays are checked for intersection with the primitives.

2) Ray Characteristics: All shading objects in DUET are considered absorbing and nonreflective, thus *reflections* off the mounting structure and frame are not captured. Since the ground is the sole reflecting surface, all rays in the simulation are deterministic and independent—an architecture that allows for parallel processing and vectorization to improve computational efficiency. This approach differs from recursive ray tracing, which can capture diffuse reflection from all defined surfaces. Recursive ray tracers follow stochastic rays away from the module to check for intersection with primitives in the scene, and each ray-primitive intersection "spawns" additional rays that emanate from the intersection point, which must also be checked for shading [46]. That process can repeat multiple times and requires significant computational resources.

DUET's deterministic rays can be classified into two groups: 1) static rays—in which all emitting sources, irradiated patches, and shading objects are stationary; and 2) dynamic rays—in which at least one of these components moves every timestamp. Fixed-tilt simulations are most computationally efficient since shading factors for diffuse and ground-reflected rays need only be calculated once in the time-independent static optical calculations in Fig. 2(b). Conversely, HSAT simulations are more computationally intensive since the predominantly dynamic rays require recalculation of shading factors each timestamp as part of the time-dependent dynamic optical calculations in Fig. 2(c).

3) Energy Transfer: DUET integrates these shading calculations with a 3-D VF model at each timestamp to predict the optical power incident on each of the cells in the module under test. The optical power on the rear of the c'th cell, $P_{c,\mathrm{r}}$, is

$$P_{c,\mathrm{r}} = \sum_{m=1}^{N_\mathrm{M}} G_{m,\mathrm{r}} \cdot A_m \tag{1}$$

where $G_{m,\mathrm{r}}$ is the *effective irradiance* incident on the rear (r) of the m'th module patch, consisting of the total incident irradiance less angle-dependent reflection losses; N_M is the number of module patches per cell and A_m is the area of the m'th module patch. The user defines the size and shape of the PV cells as well as the module patch resolution. For example, the validation in this article includes 156.75 mm pseudosquare cells, each meshed into a 4×4 grid of patches. $G_{m,\mathrm{r}}$ can be found as the sum of direct beam ($G^{\mathrm{B}}_{m,\mathrm{r}}$), diffuse sky ($G^{\mathrm{D}}_{m,\mathrm{r}}$), and ground-reflected ($G^{\mathrm{R}}_{m,\mathrm{r}}$) components

$$G_{m,\mathrm{r}} = G^{\mathrm{B}}_{m,\mathrm{r}} + G^{\mathrm{D}}_{m,\mathrm{r}} + G^{\mathrm{R}}_{m,\mathrm{r}}. \tag{2}$$

Equations analogous to (1) and (2) are used to find the effective irradiance incident on the front of the m'th module patch, $G_{m,\mathrm{f}}$, and the front (f) optical power of the c'th cell, $P_{c,\mathrm{f}}$. In the following explanation, front (f) and rear (r) subscripts are dropped to consider the irradiance incident on either side of the m'th module patch.

Direct beam effective irradiance incident on the m'th module patch is calculated as

$$G^{\mathrm{B}}_m = G_\mathrm{B} \cdot \cos\theta_{\mathrm{B},m} \cdot IAM(\theta_{\mathrm{B},m}) \cdot \delta_{\mathrm{B},m} \tag{3}$$

where $\theta_{\mathrm{B},m}$ and $\delta_{\mathrm{B},m}$ are the AOI and shading factor between the beam and the m'th module patch, respectively. *IAM* is the incidence angle modifier (IAM), governed by either the ASHRAE IAM model [47] or a user-defined sixth degree polynomial. Front and rear IAMs can be defined independently. The sun position

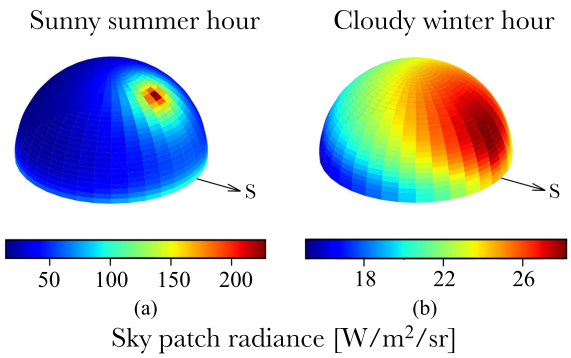

Fig. 4. Radiance of anisotropic diffuse sky based on Perez sky luminance distribution model [50] in Roskilde, Denmark during (a) a sunny 12:30 PM in summer (GHI: 851.5 $\mathrm{W/m^2}$, DHI: 126.7 $\mathrm{W/m^2}$), and (b) a cloudy 12:30 PM in winter (GHI: 73.5 $\mathrm{W/m^2}$, DHI: 71.4 $\mathrm{W/m^2}$).

is calculated with the NREL sky position algorithm [48] at the midpoint of each timestamp to accommodate timestamp-ending input data. For example, the sun position is set at 14:30 for an hourly timestamp labeled 15:00. The sun position dictates the tilt of HSAT modules, and a standard backtracking algorithm [49] adjusts HSAT module tilt away from beam normal incidence when row-to-row beam shading would otherwise be present.

Diffuse light is incident on both the front and rear of a bifacial module from a wide range of angles. DUET addresses this high angularity by meshing the entire diffuse sky dome into patches. Rays emanate from the centroid of each sky patch toward the module and ground patches. While the skydome is meshed into 36 equal azimuth divisions and 30 equal zenith divisions for the validation in this article, DUET's energy transfer framework would be compatible with an arbitrary number of mesh points and any meshing technique that provides the azimuth, zenith, and solid angles with respect to the origin.

The radiance of the s'th sky patch (L_s) is found via the 1993 Perez sky luminance distribution model [50] accounting for sky clearness, sky brightness, and the position of each patch with respect to the sun. This model generates a normalized radiance distribution for each timestamp, which is subsequently multiplied by the diffuse horizontal irradiance (DHI, or G_{D}) as shown in Fig. 4. For the timestamps when the sun is below the horizon and $G_{\mathrm{D}} > 0$, the diffuse sky is set as isotropic.

In both isotropic and anisotropic cases, the diffuse irradiance incident on the m'th module patch is calculated as

$$G_m^{\mathrm{D}} = \sum_{s=1}^{N_{\mathrm{S}}} G_s \cdot \Omega_{s,m} \cdot \cos\theta_{s,m} \cdot IAM(\theta_{s,m}) \cdot \delta_{s,m} \quad (4)$$

where N_{S} is the total number of sky patches; $\Omega_{s,m}$, $\theta_{s,m}$, $\delta_{s,m}$ are the solid angle, AOI, and shading factor between between the s'th sky patch and the m'th module patch, respectively.

Ground-reflected light is also particularly important for bifacial energy yield calculations since both energy yield and bifacial gain scale with broadband ground reflectivity, or *albedo* [4]. To represent this irradiance source, DUET divides the flat ground surface into concentric rings which are centered below the module under test, with radial dimensions increasing away from the module. These rings are meshed into equal azimuth divisions such that the solid angles between the module and all ground patches are equal, with the highest resolution patches near the module under test. The validation simulations in this article are performed with 36 azimuth and 20 radial ground divisions.

The irradiance on the g'th ground patch (G_g) is calculated as the sum of direct beam (G_g^{B}) and diffuse (G_g^{D}) irradiance

$$G_g = G_g^{\mathrm{B}} + G_g^{\mathrm{D}} \quad (5)$$

$$G_g^{\mathrm{B}} = G_{\mathrm{B}} \cdot \cos Z \cdot \delta_{\mathrm{B},g} \quad (6)$$

$$G_g^{\mathrm{D}} = \sum_{s=1}^{N_{\mathrm{S}}} L_s \cdot \Omega_{s,g} \cdot \cos\theta_{s,g} \cdot \delta_{s,g} \quad (7)$$

where Z is the zenith angle of the sun and $\delta_{\mathrm{B},g}$ is the shading factor between the beam and the ground patch; $\Omega_{s,g}$, $\theta_{s,g}$, and $\delta_{s,g}$ are the solid angle, AOI, and shading factor between the s'th sky patch and the g'th ground patch, respectively.

The ground-reflected effective irradiance on the m'th module patch can be found as

$$G_m^{\mathrm{R}} = \rho \cdot \sum_{g=1}^{N_{\mathrm{G}}} G_g \cdot \Omega_{g,m} \cdot \cos\theta_{g,m} \cdot IAM(\theta_{g,m}) \cdot \delta_{g,m} \quad (8)$$

where ρ is the albedo and N_{G} is the total number of ground patches; $\Omega_{g,m}$, $\theta_{g,m}$, $\delta_{g,m}$ are the solid angle, AOI, and shading factors between the g'th ground patch and the m'th module patch, respectively. The base version of the model assumes a Lambertian ground reflection with equal intensity in all directions and does not account for the spectral shape of reflected light.

B. Electrical Model

The short circuit current for the c'th cell under standard test conditions (STC) is determined from

$$I_{\mathrm{sc},c} = (P_{c,\mathrm{f}} + P_{c,\mathrm{r}} \cdot \varphi) \cdot \Re \quad (9)$$

where φ is the current *bifaciality* constant, which accounts for the decreased probability of carrier collection from rear-incident light, and $\Re$ is the *broadband responsivity* of the cell at STC under the Air Mass 1.5 Global spectrum (AM1.5 G) in units of A/W. While DUET's baseline model calculates performance based on AM1.5 G at all hours, the true spectrum of module-incident light varies throughout the day and year with particular dependence on geographic location [51], [52] and ground-cover [53]. In [54] and [39], a version of DUET was modified to include an AM-dependent responsivity for an encapsulated Si heterojunction module, which impacted modeled annual energy yield by 0.5%–2.5% for a latitude range of 33–69° N.

The temperature-dependent short circuit current of each cell is adjusted using

$$I_{\mathrm{sc},c}(T_c) = I_{\mathrm{sc},c} \cdot (T_{\mathrm{STC}} - T_c) \cdot \mu_{\mathrm{I}} \quad (10)$$

where μ_{I} is the temperature coefficient of current and T_{STC} is the STC temperature of 25 °C. The cell temperature, T_c, is calculated based on the sum of front and rear cell average irradiances

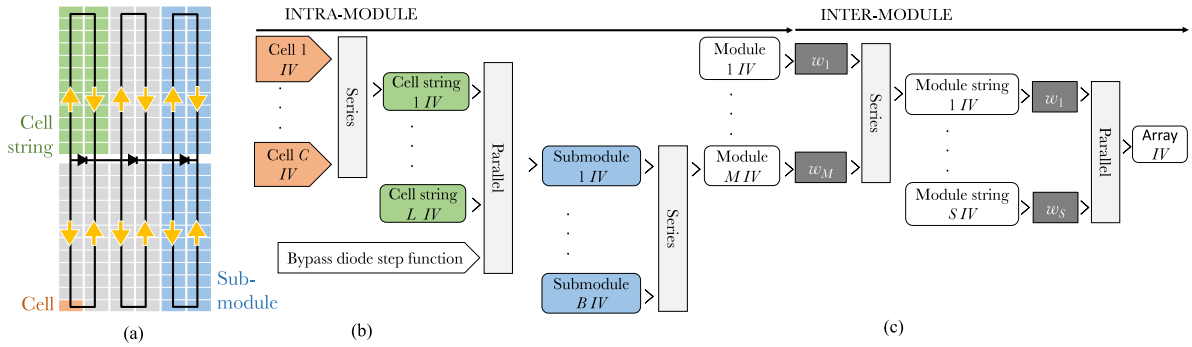

Fig. 5. (a) Intramodule wiring architecture for a half-cut cell module with cell, cell string and submodule identified, where yellow arrows indicate the direction of conventional current. (b) Electrical combination of *IV* curves within a module with *C* cells per inter-cell string, *L* inter-cell strings per submodule, and *B* submodules. (c) Intermodule *IV* curve combination with *M* modules per string and *S* module strings per array.

neglecting reflection losses ($G_{c,\mathrm{f}}, G_{c,\mathrm{r}}$)

$$G_c = G_{c,\mathrm{f}} + G_{c,\mathrm{r}} \tag{11}$$

the ambient temperature (T_a), and one of three module temperature models: the nominal operating cell temperature (NOCT) [55], Faiman [56], or Sandia [57] models. The latter two models are empirically derived functions of G_c, T_a, and wind speed.

For each timestamp, the software calculates the *IV* curve of each cell based on the single-diode model [58]

$$I_c = I_{\mathrm{sc},c}(T_c) - I_0(T_c)\exp\left[\frac{q(V_c + I_c R_\mathrm{s})}{nkT_c} - 1\right] - \frac{V_c + I_c R_\mathrm{s}}{R_\mathrm{sh}(G_c)} \tag{12}$$

where I_c and V_c are the cell current and voltage; the STC cell shunt and series resistances (R_s and R_sh), ideality factor (n), and dark saturation current (I_0) can be fit from the cell or module *IV* curves. Temperature-dependent $I_0(T_c)$ and irradiance-dependent $R_\mathrm{sh}(G_c)$ are found for each timestamp following the De Soto model approach [59].

The module *IV* curve is constructed from the combination of all cell *IV* curves based on a user-specified wiring architecture. Fig. 5(a) provides an example architecture with half-cut cells. Intermediate *IV* curves are calculated, as shown in Fig. 5(b), for: 1) strings of cells in series and 2) the parallel combination of one or more of these strings with a bypass diode into a *submodule*. Submodule *IV* curves are then combined in series to form the module *IV* curve. The flexible cell size and wiring architecture allows for simulation of emerging technologies such as large format modules with 182 or 210 mm cells or modules with multicut and shingled cells.

The series *IV* combination interpolates and sums the voltage of the cells or submodules at common current points. This procedure captures any current limitation due to the irradiance nonuniformity and could capture performance variation between cells. The parallel *IV* combination interpolates and sums current at common voltage points. As in the PVMismatch Python library [60], DUET approximates the bypass diode *IV* behavior as a step function in current at the diode's forward voltage threshold, typically ~ -0.7 V. This approach limits the negative voltage of each submodule and captures the reduced electrical mismatch loss enabled by the bypass diode. The module power under uniform average front and rear irradiance is also calculated at each timestamp to represent performance in the absence of electrical mismatch.

In 2-D VF models such as PVsyst [61], the array energy yield is estimated based on a single irradiance sample line at the center of an infinite row of modules, and the user defines loss factors to represent variations in module performance throughout the array. In DUET, users can obtain array results in a computationally efficient manner by weighting M module *IV* curves with coefficients w_1 to w_M based on the number of modules that each *IV* curve represents within a module string. As shown in Fig. 5(c), the series combination of multiple module *IV* curves generates the module string performance. The S module string *IV* curves can then be combined in parallel to form the array *IV* curve with weighting coefficients w_1 to w_S.

Importantly, this weighted summation of *IV* curves occurs *at each timestamp* allowing the extraction of maximum power of any subsection of the array at any given time. The instantaneous power is scaled by the timestamp duration to provide the energy generated during that timestamp, and the resulting time-series of output data [see Fig. 2(d)] provides insight into temporal performance variation. The summation of all timestamp energies provides the total energy yield for the module, string or array [see Fig. 2(e)].

III. Validation Methodology

A. Field Site

Results from DUET have been validated against open-access data from a bifacial PV test site in Roskilde, Denmark [see Fig. 6(a)] at 55.696°N, 12.104°E [22]. The site has 16 Soltec SF7 2P trackers: eight in HSAT configuration with north–south alignment and eight at a 25° fixed-tilt facing south. 8760 hourly on-site global horizontal irradiance (GHI), direct normal irradiance (DNI), and DHI measurements are available for April 2019–March 2020. Bifacial energy yield data is available during this period for one fixed-tilt and one HSAT row, consisting of four electrically parallel strings of 22 modules each as shown in Fig 6(b). The monthly average measured albedo ranges from 0.19 to 0.23, which did not include any periods of snow accumulation. Rear irradiance is provided from Feb. 21 to Mar. 31, 2020 as the average of two pyranometer measurements near

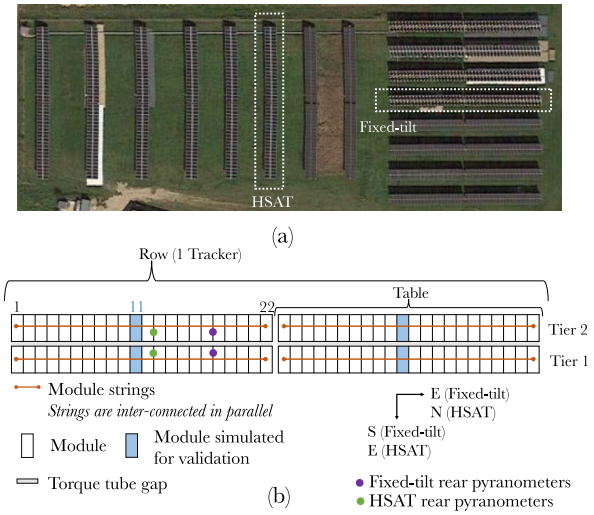

Fig. 6. (a) Satellite image of the test site in Roskilde, Denmark with measured bifacial rows in white boxes (Google Maps, Dec. 2021). (b) Physical and electrical layout of trackers and instrumentation.

the center of a table in each row of interest, on either side of the torque tube. The array geometry, including 2P mounting structure dimensions, is described further in [22]. The frameless bifacial modules are rated at 295 Watt-peak (Wp) with 60 passivated-emitter rear contact (PERC) cells and a bifaciality constant of 0.67. Module temperature coefficients and *IV* curves are available in the datasheet [62].

Riedel-lyngskaer *et al.* [1] provided an in-depth comparison of results from eight bifacial PV performance models against the measured rear irradiance data from this site: MoBiDiG Hybrid [8] with ray tracing based on bifacial_radiance [9], [23], MoBiDiG VF [24], PlantPredict [31], PVsyst [32], systems advisory model (SAM) [30], SolarFarmer [27], bifacialvf [6], and pvfactors [7]. In Section IV-C, we compare DUET's rear irradiance error to results in [1] for these software. We do not provide a direct comparison of energy yield error due to a 5-min time shift discovered in the measured power data after publication of [1]. The present validation compares DUET's modeled energy yield to Version 3 of the open-access data [22], whereas error values in [1] are based on a previous version of that dataset.

B. Simulation

The electrical stringing configuration in Fig. 6(b) shows that all modules within a module string are on the same tier and share the same ground clearance. Thus, we assume that the modules along the table share similar irradiance profiles, neglecting edge effects, and pilings for this validation. We simulated one module per string, shown in blue in Fig. 6(b), and multiplied its *IV* curve by 22 to get four module string *IV* curves. The results from these four strings were combined to find the energy of the row and then compared to the measured row yield. The electrical calculations were repeated for the three module temperature models—NOCT (44 °C [62]), Faiman, and Sandia. The Faiman model coefficients used are $U_0 = 31.0\ \mathrm{W/(m^2\,K)}$ and $U_1 = 1.6\ \mathrm{W\,s/(m^3\,K)}$ as derived by Soltec for this tracker at a site in California [63], and the Sandia coefficients are set for a glass-cell-glass module with open racking. Since seven of the eight models in [1] use the Faiman model, we present energy yield results for the Faiman model in the following sections, unless otherwise stated.

For comparison to measurements, we place an irradiance "sensor" sample point at the 3-D coordinate of each pyranometer [see Fig. 6(b)]. The piling adjacent to the fixed-tilt pyranometers is also modeled. The two-sensor average without IAM is then compared to the rear irradiance measurement, which is provided as the average of pyranometer irradiances.

C. Analysis

The analysis in [1] filters timestamps based on the following four criteria.

1) Sun elevation greater than 5°.
2) Tracker angle agreement between rows.
3) Availability of data acquisition systems.
4) Lack of morning shade on the bifacial HSAT.

For the sake of comparison, the present analysis also uses these same criteria, resulting in a total of 3370 energy timestamps for fixed-tilt and 2371 energy timestamps for HSAT. Filtered rear irradiance measurements are available for 375 and 207 timestamps for fixed-tilt and HSAT, respectively. The following sections compare modeled results (y) to measured data (x) over these sets of hourly timestamps using the metrics of relative error, MAE and mean bias error (MBE)

$$\text{Relative error} = \frac{\sum_{i=1}^{N} y_i}{\sum_{i=1}^{N} x_i} - 1 \tag{13}$$

$$\text{MAE} = \frac{1}{N}\sum_{i=1}^{N} |(y_i - x_i)| \tag{14}$$

$$\text{MBE} = \frac{1}{N}\sum_{i=1}^{N} (y_i - x_i) \tag{15}$$

where N is the number of timestamps.

IV. Results and Discussion

A. General Performance

Fig. 7 shows a comparison of modeled and measured data over the filtered timestamps for bifacial energy and rear insolation in the fixed-tilt [see Fig. 7(a), (b)] and HSAT [see Fig. 7(c), (d)] rows of interest. The blue and orange lines in each subplot represent the linear fit and perfect 1:1 lines, respectively, between DUET's modeled data and the measured data. The R^2 value for DUET's bifacial energy yield prediction is 0.995 or greater for both arrays, indicating good agreement with measurement. The modeled bifacial energy yield is 1.56% lower than measured data for fixed-tilt and 0.72% lower for HSAT. This relative error is less than the 4.5% combined uncertainty of summer clear sky hourly GHI and dc power measurements estimated in [1], as was the case for the six software simulating energy yield at the Roskilde site in that publication.

Modeled rear insolation in Fig. 7(b) and (d) also shows close agreement to pyranometer data with an R^2 of 0.987 for fixed-tilt

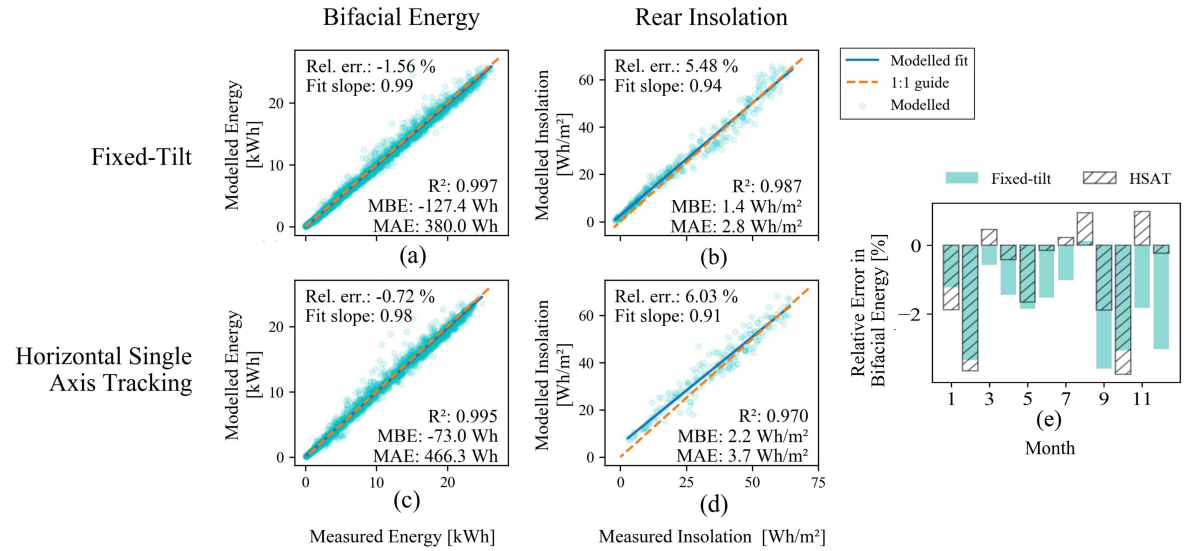

Fig. 7. Comparison of results modeled in DUET as a function of measured data for (a) fixed-tilt bifacial energy yield, (b) fixed-tilt rear insolation, (c) HSAT bifacial energy yield, and (d) HSAT rear insolation at the Roskilde, Denmark field site. Rel. err. = relative error. (e) Monthly relative error in DUET's modeled bifacial energy yield for fixed-tilt and HSAT systems. Energy reported here is modeled using the Faiman module temperature model.

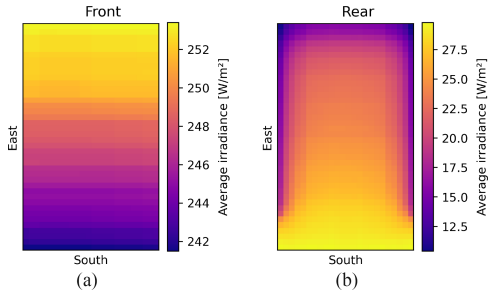

Fig. 8. Irradiance profiles for a frameless southern module in the fixed-tilt system, as generated by DUET. Average effective irradiance over 3370 hourly timestamps for the (a) front and (b) rear of the module.

and 0.970 for HSAT but overestimates in the many low irradiance hours resulting in 5.5% and 6.0% relative error, respectively. This low-irradiance overestimation is also present for all models in [1]. The hours with measured fixed-tilt rear insolation < 20 $\mathrm{Wh/m^2}$ have an average diffuse fraction of 86%, and 51% of these hours have DNI < 1, where diffuse shading from adjacent buildings or trees could have a significant impact. Relative humidity also rises to 82.2% in these low DNI hours producing the necessary conditions for rain and fog, which may impact ground-reflected light.

B. Irradiance Nonuniformity

With multiple sample points across the length and width of each cell, DUET's 2-D irradiance profiles capture nonuniformity across the full front and rear surfaces of the module. For example, Fig. 8(a) shows that modeled average front irradiance differs between the top and bottom of a southern module in the fixed-tilt row by approximately 13.2 $\mathrm{W/m^2}$. The irradiance gradient—primarily induced by inter-row diffuse shading—is relatively constant across the width of this module and could be represented by sampling a cross-section of irradiance down the center. In contrast, the rear irradiance profile in Fig. 8(b) shows shading on the sides and top due to the supporting purlins and torque tube, which would not be captured by cross-sectional irradiance sampling and which introduces a 18.0 $\mathrm{W/m^2}$ difference in average irradiance between the brightest and most shaded module patches.

While Fig. 8 shows an average irradiance profile across all filtered timestamps, DUET calculates energy yield based on a unique 2-D irradiance profile at each timestamp, thus capturing the temporal specificity of intercell current mismatch that cannot be represented by an annualized loss factor. In October to December, the monthly relative error between modeled and measured fixed-tilt energy yield drops from 6.6–9.2% to between -1.8% and -3.1% when current mismatch loss between cells is activated within DUET. These months feature many hours of low sun elevation when adjacent rows partially obscure the direct beam, and this significant error reduction indicates that DUET represents the resulting intercell current mismatch well. Overall, relative error for both fixed-tilt and HSAT ranges from $<1\%$ in magnitude in March to -3.75% in October [see Fig. 7(e)]—lower than the $>10\%$ fixed-tilt and $>5\%$ HSAT monthly error reported for some models in [1].

C. Cross-Software Comparison

The range of rear average insolation MAE for the eight other models is taken from the text of [1] and replotted as the light blue bars in Fig. 9(a). The MAE values in that paper were averaged over the filtered hourly timestamps and include the effect of an IAM as well as Soltec's recommended +0.7% shading factor [63] for the VF models. DUET's rear module irradiance sits within this range, both with and without an IAM applied, although close agreement with pyranometer data is not expected due to rack shading that does not affect the measurement device. The "sensor" approach samples the rear irradiance using the

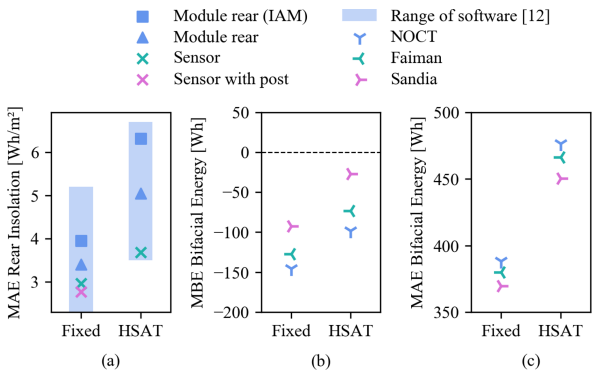

Fig. 9. Performance statistics for DUET and software from previous study [1] as compared to on-site measured data for fixed-tilt and HSAT systems. (a) MAE in modeled rear insolation. (b) MBE and (c) MAE in modeled bifacial energy yield for three temperature models. Wp = Watt peak (25.96 kW).

locations and size of the pyranometer, showing lower MAE than the module average by 0.44 $\mathrm{W/m^2}$ for fixed-tilt and 1.37 $\mathrm{W/m^2}$ for HSAT. The addition of the post adjacent to the fixed-tilt pyranometers further improves the MAE by 0.18 $\mathrm{W/m^2}$.

DUET's bifacial energy yield with the NOCT module temperature model shows an MBE of −146 Wh and −98 Wh for fixed-tilt and HSAT, respectively [see Fig. 9(b)]. This underestimation is partly due to module temperature overestimation, since accounting for wind cooling in the Faiman and Sandia models decreases the MBE magnitude by 18.3 and 53.0 Wh, respectively. The resulting MAE falls within 370–388 Wh (14.2–15.0 mW/Wp) for all three temperature models in fixed-tilt and 450–477 Wh (17.3–18.3 mW/Wp) in HSAT. When DUET's modeled energy yield error is calculated using measured data without the 5-min correction outlined in Section III-A, the resulting MAEs are lower than those reported for the six models in [1] by 23–107 Wh for fixed-tilt and 29–90 Wh for HSAT. The 5-min correction reduces DUET's MAE by 86 and 10.5 Wh, respectively. If we assume a similar corrective behavior for all models, DUET performs with lowest cumulative absolute error across all timestamps for both systems.

V. Conclusion

This article has presented a technical description of a new bifacial PV performance software, DUET, including a mathematical representation of optical and electrical numerical models. The novel shading algorithm combines a 3-D VF model with ray-object intersection to capture the effect of supportive structure shading, and the *IV* curve summation flexibly represents intra- and intermodule wiring and electrical mismatch loss between cells, modules, and module strings.

A validation against measured data from Denmark [22] shows that DUET predicts bifacial energy yield at −1.56% of measured yield for a fixed-tilt row over 3370 daylight hours and at −0.72% of measured yield for a HSAT row over 2731 daylight hours. The resulting MAE in bifacial power across the simulated daylight hours is 14.2–15.0 mW/Wp for fixed-tilt and 17.3–18.3 mW/Wp for HSAT, depending on the module temperature model. DUET's electrical model captures current mismatch due to irradiance nonuniformity, including partial direct beam shading during periods of low sun elevation in the fixed-tilt system. 2-D rear irradiance profiles also display nonuniformity caused by supportive racking that cannot be captured in a cross-sectional sample of module irradiance. For the subset of hours in which

TABLE I
List of Symbols

G_{H}	Global horizontal irradiance	$\mathrm{W/m^2}$
G_{B}	Direct normal (beam) irradiance	$\mathrm{W/m^2}$
G_{D}	Diffuse horizontal irradiance	$\mathrm{W/m^2}$
ρ	Albedo	unitless
N_{S}	Number of (No.) sky patches	unitless
N_{G}	No. ground patches	unitless
N_{M}	No. module patches per cell	unitless
e	Emitting source	-
i	Irradiated patch	-
$\delta_{e,i}$	Shading factor between e and i	unitless
$\theta_{e,i}$	Angle of incidence between e and i	°
$\Omega_{e,i}$	Solid angle between e and i	sr
c	Cell number	-
m	Module patch number	-
s	Sky patch number	-
g	Ground patch number	-
$P_{c,\mathrm{f}}$	Optical power on front of cell c	W
$P_{c,\mathrm{r}}$	Optical power on rear of cell c	W
A_m	Area of module patch m	$\mathrm{m^2}$
$G_{m,\mathrm{r}}$	Effective irradiance on rear of module patch m, including reflection losses	$\mathrm{W/m^2}$
G_m^{B}	Direct beam effective irradiance on module patch m, including reflection losses	$\mathrm{W/m^2}$
G_m^{D}	Diffuse effective irradiance on module patch m, including reflection losses	$\mathrm{W/m^2}$
G_m^{R}	Ground-reflected effective irradiance on module patch m, including reflection losses	$\mathrm{W/m^2}$
$G_{c,\mathrm{f}}$	Average irradiance on front of cell c neglecting reflection losses	$\mathrm{W/m^2}$
$G_{c,\mathrm{r}}$	Average irradiance on rear of cell c neglecting reflection losses	$\mathrm{W/m^2}$
G_c	Total average irradiance incident on both sides of cell c neglecting reflection losses	$\mathrm{W/m^2}$
L_s	Radiance of sky patch s	$\mathrm{W/m^2/sr}$
G_g	Irradiance incident on ground patch g	$\mathrm{W/m^2}$
Z	Sun zenith	°
$\Re$	Cell responsivity at STC	A/W
φ	Current bifaciality constant	unitless
$I_{\mathrm{sc},c}$	Short circuit current of cell c	A
I_c	Current of cell c	A
V_c	Voltage of cell c	V
q	Elementary charge	C
k	Boltzmann's constant	J/°C
n	Cell ideality factor at STC	unitless
I_0	Cell saturation current at STC	A
R_{sh}	Cell shunt resistance at STC	Ω
R_{s}	Cell shunt resistance at STC	Ω
T_{a}	Ambient temperature	°C
μ_{I}	Current temperature coefficient	%/°C
T_{STC}	Temperature at standard test condition	°C
T_c	Temperature of c	°C
w_M	Weighting coefficient of M'th module *IV*	No. modules
w_S	Weighting coefficient of S'th module string *IV*	No. strings

TABLE II
ADDITIONAL USER-DEFINED INPUTS

	Input	Unit or Option
Geo	Longitude	° (E>0)
	Latitude	° (N>0)
	Time zone	from UTC (E>0)
Array	Number of (No.) rows	-
	Pitch (row spacing)	m
	Array azimuth	° (S=0; E>0)
Table	Location of module	row, tier, column of the array
	Module orientation	portrait, landscape
	Torque tube shape	cylinder, rectangular prism
	Torque tube dimensions	m (radius or cross-sectional edges)
	Purlin shape, dimensions	rectangular prism, polygons ; m
	Pile shape	cylinder, rectangular prism
	Pile position, dimensions	m
	Tracker angle bounds	°, e.g. ±60
	Backtracking	on, off
Module	Cell type	full, half-cut, multi-cut
	Cell shape, dimensions	pseudo-square, rectangle; m
	Cell material bandgap	eV (e.g., 1.121 for Si)
	Bandgap temp. coeff.	%/°C
	No. cells, bypass diodes (BD)	-
	No. cell strings per BD	-
	Cell gap, margins	m (between cells, from edges)
	Incidence angle modifier	polynomial, ASHRAE [47]
	Module frame dimensions	m

*UTC = Coordinated Universal Time; temp. coeff. = temperature coefficient.

rear irradiance measurements were provided, the modeled irradiance at the location of two rear-facing pyranometers matches the measured data within 2.8 $\mathrm{W/m^2}$ for the fixed-tilt row and 3.7 $\mathrm{W/m^2}$ for the HSAT row—among the lowest errors reported for other software tested at this site in [1].

This article shows that DUET's shading algorithm performs with similar accuracy to other bifacial performance models—including a ray tracing model—while minimizing computational cost through deterministic ray-object intersections. With this approach, DUET provides computationally efficient bifacial performance modeling with geographic, temporal, and structural specificity—without reliance on estimated shading and electrical mismatch loss factors. The software can also be used to acquire, and better understand, such loss factors for use in other performance models or in system design optimization.

ACKNOWLEDGMENT

The authors would like to thank Henry P. Schriemer and Chu Tu Li for original concept work and early discussions, Nicholas Riedel-Lyngskær for correspondence regarding the Roskilde dataset, and Jill Tymchak for help with early validation. The University of Ottawa is on unceded Algonquin Territory. They recognize Indigenous self-determination as central to addressing climate change.

APPENDIX

A. Computation Time and Modeled Data

The HSAT annual energy yield calculations herein required 3.75 core-hours per module on a 3.9 GHz CPU. In general, DUET's computation time strongly depends on tracking type, patching resolution, size of array, and number of shading elements. Considerable speed improvements are expected through ongoing code refinements and improved algorithms.

The modeling results presented in this article are available for download in [64].

REFERENCES

[1] N. Riedel-lyngskaer et al., "Validation of bifacial photovoltaic simulation software against monitoring data from large-scale single-axis trackers and fixed tilt systems in Denmark," *Appl. Sci.*, vol. 10, no. 23, pp. 1–29, 2020.
[2] C. D. Rodríguez-Gallegos et al., "Global techno-economic performance of bifacial and tracking photovoltaic systems," *Joule*, vol. 4, pp. 1–28, 2020.
[3] R. Kopecek and J. Libal, "Towards large-scale deployment of bifacial photovoltaics," *Nature Energy*, vol. 3, no. 6, pp. 443–446, 2018.
[4] A. Asgharzadeh et al., "A sensitivity study of the impact of installation parameters and system configuration on the performance of bifacial PV arrays," *IEEE J. Photovolt.*, vol. 8, no. 3, pp. 798–805, May 2018.
[5] J. R. Ledesma et al., "A simulation model of the irradiation and energy yield of large bifacial photovoltaic plants," *Sol. Energy*, vol. 206, pp. 522–538, 2020. [Online]. Available: https://doi.org/10.1016/j.solener.2020.05.108
[6] B. Marion et al., "A practical irradiance model for bifacial PV modules," in *Proc. IEEE 44th Photovolt. Specialists Conf.*, 2017, pp. 1537–1542.
[7] M. A. Anoma et al., "View factor model and validation for bifacial pv and diffuse shade on single-axis trackers," in *Proc. IEEE 44th Photovolt. Specialist Conf.*, 2018, pp. 1549–1554.
[8] D. Berrian and J. Libal, "A comparison of ray tracing and view factor simulations of locally resolved rear irradiance with the experimental values," *Prog. Photovolt., Res. Appl.*, vol. 28, no. 6, pp. 609–620, 2020.
[9] S. A. Pelaez, C. Deline, P. Greenberg, J. S. Stein, and R. K. Kostuk, "Model and validation of single-axis tracking with bifacial PV," *IEEE J. Photovolt.*, vol. 9, no. 3, pp. 715–721, May 2019.
[10] K. R. McIntosh et al., "Simulation and measurement of monofacial and bifacial modules in a 1D tracking system," in *Proc. Conf. Rec. IEEE Photovolt. Specialists Conf.*, 2020, pp. 0366–0370.
[11] C. K. Lo, Y. S. Lim, and F. A. Rahman, "New integrated simulation tool for the optimum design of bifacial solar panel with reflectors on a specific site," *Renewable Energy*, vol. 81, pp. 293–307, 2015. [Online]. Available: http://dx.doi.org/10.1016/j.renene.2015.03.047
[12] J. S. Stein et al., "Bifacial PV modules & systems: Experience and results from international research and pilot applications. international energy agency photovoltaic power systems programme," 2021. [Online]. Available: https://iea-pvps.org/wp-content/uploads/2021/04/IEA-PVPS-T13-14_2021-Bifacial-Photovoltaic-Modules-and-Systems-report.pdf
[13] A. Driesse and N. Patel, "Cross-validation of PV system simulation software," in *Proc. 35th Eur. Photovolt. Sol. Energy Conf. Exhib.*, 2019, pp. 9–13.
[14] M. Chiodetti, J. Kang, C. Reise, and A. Lindsa, "Predicting yields of bifacial PV power plants – what accuracy Is possible?," in *Proc. 35th Eur. Photovoltaic Sol. Energy Conf. Exhib.*, 2018, pp. 1623–1629. [Online]. Available: https://www.eupvsec-proceedings.com/proceedings?paper=45942
[15] A. Asgharzadeh et al., "A benchmark and validation of bifacial PV irradiance models," in *Proc. IEEE 46th Photovolt. Specialists Conf.*, 2019, pp. 3281–3287.
[16] T. Capelle, F. Araya, F. Haffner, J. Sayritupac, and H. Colin, "A comparison of bifacial PV system modelling tools," in *6th BifiPV Workshop. Amsterdam: INES France*, 2019. [Online]. Available: http://npv-workshop.com/fileadmin/layout/images/bifiPV/presentations2019/bifiPV2019-CEA_INES_Capelle.pdf
[17] C. Zhao, J. Xiao, Y. Yu, and J.-N. Jaubert, "Accurate shading factor and mismatch loss analysis of bifacial HSAT systems through ray-tracing modeling," *Sol. Energy Adv.*, vol. 1, 2021, Art. no. 100004. [Online]. Available: https://doi.org/10.1016/j.seja.2021.100004
[18] M. Ernst, G. E. Conechado, and C.-A. Asselineau, "Accelerating the simulation of annual bifacial illumination of real photovoltaic systems with ray tracing," *iScience*, vol. 25, no. 1, 2021, Art. no. 103698. [Online]. Available: https://doi.org/10.1016/j.isci.2021.103698
[19] H. Nussbaumer et al., "Accuracy of simulated data for bifacial systems with varying tilt angles and share of diffuse radiation," *Sol. Energy*, vol. 197, 2019, pp. 6–21, 2020. [Online]. Available: https://doi.org/10.1016/j.solener.2019.12.071
[20] S. Ayala Peláez, "BEST field data—data and resources," 2021. [Online]. Available: https://datahub.duramat.org/dataset/best-field-data

[21] S. Ayala Pelaez, C. Deline, S. M. MacAlpine, and W. Marion, "Bifacial PV test-bed irradiance measurements," 2019. [Online]. Available: https://data.nrel.gov/submissions/125

[22] N. Riedel et al., "Data used in "validation of bifacial photovoltaic simulation software against monitoring data from large-scale single-axis trackers and fixed tilt systems in Denmark," 2021. [Online]. Available: https://doi.org/10.11583/DTU.13580759.v3

[23] S. A. Pelaez et al., "Comparison of bifacial solar irradiance model predictions with field validation," *IEEE J. Photovolt.*, vol. 9, no. 1, pp. 82–87, Jan. 2019.

[24] D. Berrian, J. Libal, M. Klenk, H. Nussbaumer, and R. Kopecek, "Performance of bifacial PV arrays with fixed tilt and horizontal single-axis tracking: Comparison of simulated and measured data," *IEEE J. Photovolt.*, vol. 9, no. 6, pp. 1583–1589, Nov. 2019.

[25] O. A. Katsikogiannis, H. Ziar, and O. Isabella, "Integration of bifacial photovoltaics in agrivoltaic systems: A synergistic design approach," *Appl. Energy*, vol. 309, no. Dec. 2021, Art. no. 118475. [Online]. Available: https://doi.org/10.1016/j.apenergy.2021.118475

[26] M. F. Cohen, D. P. Greenberg, D. S. Immel, and P. J. Brock, "An efficient radiosity approach for realistic image synthesis," *IEEE Comput. Graph. Appl.*, vol. 6, no. 3, pp. 26–35, Mar. 1986.

[27] M. A. Mikofski, R. Darawali, M. Hamer, A. Neubert, and J. Newmiller, "Bifacial performance modeling in large arrays," in *Proc. Conf. Rec. IEEE Photovolt. Specialists Conf.*, 2019, pp. 1282–1287.

[28] C. D. Rodríguez-Gallegos et al., "Monofacial vs bifacial Si-based PV modules: Which one is more cost-effective?," *Sol. Energy*, vol. 176, pp. 412–438, 2018. [Online]. Available: https://doi.org/10.1016/j.solener.2018.10.012

[29] M. Rouholamini, L. Chen, and C. Wang, "Modeling, configuration, and grid integration analysis of bifacial PV arrays," *IEEE Trans. Sustain. Energy*, vol. 12, no. 2, pp. 1242–1255, Apr. 2021.

[30] P. Gilman et al., "SAM PV model technical reference update," Nat. Renewable Energy Lab., Golden, CO, USA, Tech. Rep. NREL/TP-6A20-67399, 2018.

[31] Plant Predict Resource Centre, "Bifacial Modules," 2021. [Online]. Available: https://plantpredict.com/algorithm/irradiance-radiation/679-2/

[32] B. Wittmer, "Simulating bifacial fixed tilt and tracking systems with PVsyst," in *PV Mag. Webinar*, 2019. [Online]. Available: https://www.pvmagazine.com/webinars/pv-magazine-webinar-optimizing-bifacial-gain-and-balancinginvestment-costs/

[33] W. Gu, T. Ma, M. Li, L. Shen, and Y. Zhang, "A coupled optical-electrical-thermal model of the bifacial photovoltaic module," *Appl. Energy*, vol. 258, 2020, Art. no. 114075. [Online]. Available: https://doi.org/10.1016/j.apenergy.2019.114075

[34] K. R. McIntosh, M. D. Abbott, and B. A. Sudbury, "How the PVSyst inputs for bifacial systems depend on conditions," in *Proc. 7th bifiPV (virtual)*, 2020. [Online]. Available: https://www.dropbox.com/s/o4cx2xk3slastgl/T6A.-Keith.pdf?dl=0

[35] A. Burgers and B. van Aken, "BIGEYE–Simulation under shadow conditions," in *BifiPV Workshop*, Amsterdam, The Netherlands. 2019. [Online]. Available: http://npv-workshop.com/fileadmin/layout/images/bifiPV/presentations2019/bifiPV2019-_TNO_ECN_-_Burgers.pdf

[36] E. Barros, B. Van Aken, A. Burgers, L. Slooff-Hoek, and R. Fonseca, "Multi-objective optimization of solar park design under climatic uncertainty," *Sol. Energy*, vol. 231, pp. 958–969, 2022. [Online]. Available: https://doi.org/10.1016/j.solener.2021.12.026

[37] U. A. Yusufoglu et al., "Simulation of energy production by bifacial modules with revision of ground reflection," *Energy Procedia*, vol. 55, pp. 389–395, 2014. [Online]. Available: http://dx.doi.org/10.1016/j.egypro.2014.08.111

[38] D. Chudinzow, J. Haas, G. Díaz-Ferrán, S. Moreno-Leiva, and L. Eltrop, "Simulating the energy yield of a bifacial photovoltaic power plant," *Sol. Energy*, vol. 183, pp. 812–822, 2019. [Online]. Available: https://doi.org/10.1016/j.solener.2019.03.071

[39] M. R. Lewis et al., "Impact of air mass on energy yield calculation for bifacial silicon heterojunction photovoltaic modules in high-latitude conditions," in *Proc. Conf. Rec. IEEE Photovolt. Specialists Conf.*, 2020, pp. 0371–0375.

[40] C. E. Valdivia et al., "Bifacial photovoltaic module energy yield calculation and analysis," in *Proc. IEEE 44th Photovolt. Specialists Conf.*, 2017, pp. 1094–1099.

[41] C. T. Li, "Development of field scenario ray tracing software for the analysis of bifacial photovoltaic solar panel performance," Univ. Ottawa, Ottawa, ON, Canada, 2016. [Online]. Available: http://www.ruor.uottawa.ca/handle/10393/35523

[42] T. Moller and E. Haines, "Ray/Box Intersection - Intersection Test Methods," in *Real-Time Rendering*, 2nd ed. Natick, MA, USA: AK Peters/CRC Press, 2002, pp. 572–578.

[43] A. Williams, S. Barrus, R. K. Morley, and P. Shirley, "An efficient and robust ray-box intersection algorithm," *J. Graph. Tools*, vol. 10, no. 1, pp. 49–54, 2005.

[44] D. Sunday, "Line segment and convex polygon intersection," in *Practical Geometric Algorithms With C Code*, 2021. [Online]. Available: www.geomalgorithms.com/

[45] D. Sunday, "dist3D_Segment_to_Segment," in *Practical geometric algorithms with c code*, 2021. [Online]. Available: https://www.geomalgorithms.com/

[46] P. Shirley, "Global Illumination," in *Fundamentals of Computer Graphics*, 1st ed. Wellesley, MA, USA: A. K. Peters, 2005, ch. 23, pp. 551–560.

[47] A. F. Souka and H. H. Safwat, "Determination of the optimum orientations for the double-exposure, flat-plate collector and its reflectors," *Sol. Energy*, vol. 10, no. 4, pp. 170–174, 1966.

[48] I. Reda and A. Andreas, "Solar position algorithm for solar radiation applications (revised)," Nat. Renewable Energy Lab., Golde, CO, USA, Tech. Rep. NREL/TP-560-34302, 2005. [Online]. Available: https://www.nrel.gov/docs/fy08osti/34302.pdf

[49] E. Lorenzo, L. Narvarte, and J. Muñoz, "Tracking and back-tracking," *Prog. Photovolt., Res. Appl.*, vol. 19, no. 6, pp. 747–753, 2011.

[50] R. Perez, R. Seals, and J. Michalsky, "All-weather model for sky luminance distribution-preliminary configuration and validation," *Sol. Energy*, vol. 50, no. 3, pp. 235–245, 1993.

[51] K. A. Klise, C. W. Hansen, and J. S. Stein, "Dependence on geographic location of air mass modifiers for photovoltaic module performance models," in *Proc. IEEE 42nd Photovolt. Specialist Conf.*, 2015, pp. 1–5.

[52] E. M. Tonita et al., "Effect of air mass on carrier losses in bifacial silicon heterojunction solar cells," *Sol. Energy Mater. Sol. Cells*, vol. 230, 2021, Art. no. 111293. [Online]. Available: https://doi.org/10.1016/j.solmat.2021.111293

[53] N. Riedel-Lyngskær et al., "The effect of spectral albedo in bifacial photovoltaic performance," *Sol. Energy*, vol. 231, no. 2021, pp. 921–935, 2022.

[54] M. R. Lewis, "Performance of silicon heterojunction cells and modules in arctic applications: Impact of angle of incidence, Air Mass, and Spectra on Energy Yield," Univ. Ottawa, 2020. [Online]. Available: https://ruor.uottawa.ca/handle/10393/41164

[55] G. M. Masters, "Temperature-related PV derating," in *Renewable Efficient Electric Power Syst.*, 2nd ed. Piscataway, NJ, USA: Wiley, 2013, ch. 6.3.2, pp. 327–330.

[56] D. Faiman, "Assessing the outdoor operating temperature of photovoltaic modules," *Prog. Photovolt., Res. Appl.*, vol. 16, no. 1, pp. 307–315, 2008. [Online]. Available: https://doi.org/10.1002/pip.813

[57] D. L. King, J. a. Kratochvil, and W. E. Boyson, "Photovoltaic array performance model," *Online*, vol. 8, pp. 1–19, 2004. [Online]. Available: http://mauisolarsoftware.com/MSESC/PerfModel2003.pdf

[58] J. L. Gray, "The physics of the solar cell," in *Handbook of Photovoltaic Science and Engineering*,, 2nd ed., A. Luque and S. Hegedus, Eds. Hoboken, NJ, USA: Wiley, 2011, ch. 3.

[59] W. De Soto, S. A. Klein, and W. A. Beckman, "Improvement and validation of a model for photovoltaic array performance," *Sol. Energy*, vol. 80, no. 1, pp. 78–88, 2006.

[60] SunPower, "PVMismatch v4.1 Documentation," 2017. [Online]. Available: https://sunpower.github.io/PVMismatch/

[61] A. Mermoud and B. Wittmer, "Yield simulations for horizontal axis trackers with bifacial PV modules in PVsyst," in *Proc. 35th Eur. Photovoltaic Sol. Energy Conf.*, 2018, pp. 1929–1934. [Online]. Available: 10.4229/35thEUPVSEC 20182018--6CV.2.19

[62] Trina Solar"DUOMAX Twin 295-310 W," TSM-DEG5C.20(II), 2018.

[63] J. G. Pérez and J. N. Berbel, "BiTEC : How to simulate bifacial projects?," Soltec, Tech. Rep. BiTEC Results 2 - Fall 2018 . Winter 2019, 2019. [Online]. Available: https://lab.soltec.com/bifacial-trackers-ii/

[64] A. C. J. Russell, C. E. Valdivia, C. Bohémier, J. E. Haysom, and K. Hinzer, "Modelled data in "DUET: A novel energy yield model with 3D shading for bifacial photovoltaics systems," 2022. [Online]. Available: https://doi.org/10.5683/SP3/HLZ6JG